GEOPHYSICS, VOL. 74, NO. 2 (MARCH-APRIL 2009); P. B23–B36, 15 FIGS., 1 TABLE.
10.1190/1.3072620

Case History

Imaging a hydrate-related cold vent offshore Vancouver Island from deep-towed multichannel seismic data

Tao He[1,2], George D. Spence[2], Warren T. Wood[3], Michael Riedel[4], and Roy D. Hyndman[5,2]

ABSTRACT

The Bullseye vent, an approximately 500-m-diameter deep-sea, hydrate-related cold vent on the midslope offshore Vancouver Island, was imaged in a high-resolution multichannel survey by the Deep-towed Acoustics and Geophysics System (DTAGS) The structure was drilled by the Integrated Ocean Drilling Program at site U1328. Towed about 300 m above the seafloor, the high-frequency (220–820 Hz) DTAGS system provides a high vertical and lateral resolution image. The major problems in imaging with DTAGS data are nonlinear variations of the source depths and receiver locations. The high-frequency, short-wavelength data require very accurate positioning of source and receivers for stacking and velocity analyses. New routines were developed for optimal processing, including receiver cable geometry estimation from node depths, direct arrivals and sea-surface reflections using a genetic algorithm inversion method, and acoustic image stitching based on relative source positioning by crosscorrelating redundant data between two adjacent shots. Semblance seismic velocity analysis was applied to common-reflection-point bins of the corrected data. The processed images resolve many subvertical zones of low seismic reflectivity and fine details of subseafloor sediment structure. At the Bullseye vent, where a 40-m-thick near-surface massive hydrate layer was drilled at U1328, the images resolve the upper part of the layer as a dipping high-reflectivity zone, likely corresponding to a fracture zone. Velocity analyses were not possible in the vent structure but were obtained 180–270 m to either side. Normal velocities are in the upper 50 m, but over the interval from 50 to 100 m below the seafloor at the northeast side, the velocities are higher than the average normal slope sediment velocity of approximately 1590 m/s. These high velocities are probably related to the high reflectivity zone and to the bottom portion of the massive hydrate detected by resistivity measurements in the upper 40 m at U1328.

INTRODUCTION

At the northern Cascadia margin, the incoming subducting sedimentary cover is almost completely scraped off the oceanic plate at the deformation front along thrusts that extend down near the top of the ocean crust, forming a large accretionary prism (Davis and Hyndman, 1989). Within the accretionary prism off Vancouver Island, a cold vent field in the midslope region has been studied intensively since 1999, using many geophysical, geological, and geochemical techniques. The most prominent vent, the Bullseye structure, has a diameter of approximately 500 m. It was drilled by the Integrated Ocean Drilling Program (IODP) at site U1328 (Riedel et al., 2006a), as shown in Figures 1 and 2, where high concentrations of gas hydrate were detected on downhole logs and recovered at depths of about 5–40 m below the seafloor (mbsf).

The cold vent field is located on a bathymetric bench at 1200–1400 m depth. IODP site U1328 and nearby Ocean Drilling Program (ODP)/IODP sites 889/U1327 were located near a topographic high on this bench (Figure 1). All sediments consist of silty clays and clayey silts interbedded with fine sand turbidities (Westbrook et al., 1994). Deformed, compacted, and partially cemented Cascadia Basin sediments are found below 128 mbsf at site U1327. Little-deformed slope sediments are found above 128 mbsf at U1327 and above 300 m at U1328 (Riedel et al. , 2006a).

Manuscript received by the Editor 24 May 2008; revised manuscript received 18 October 2008; published online 20 February 2009.
[1]Peking University, School of Earth and Space Sciences, Key Laboratory of Orogenic Belts and Crustal Evolution, MOE, Beijing, China. E-mail: taohe@pku.edu.cn.
[2]University of Victoria, School of Earth and Ocean Sciences, Victoria, British Columbia, Canada. E-mail: taohe@uvic.ca; gspence@uvic.ca.
[3]Naval Research Laboratory, Stennis Space Center, Mississippi, U.S.A. E-mail: warren.wood@nrlssc.navy.mil.
[4]McGill University, Department of Earth and Planetary Sciences, Montreal, Canada. E-mail: mriedel@eps.mcgill.ca.
[5]Geological Survey of Canada, Pacific Geoscience Centre, Sidney, British Columbia, Canada. E-mail: RHyndman@NRCan.gc.ca.

The Cascadia accretionary margin contains one of the most comprehensively studied occurrences of marine gas hydrate. Offshore Vancouver Island, a hydrate bottom-stimulating reflection (BSR) occurs over much of a 30-km-wide band parallel to the coast beneath the midcontinental slope (Figure 1a). As one end member for hydrate formation, methane is removed from regional diffusive upward fluid flow driven by tectonic compression (Hyndman and Davis, 1992; Haacke et al., 2008b). In these models, the regional concentration of gas hydrate gradually decreases upward from a maximum near the base of the gas hydrate stability zone (GHSZ). However, recent results from expedition 311 show that the hydrate distribution is very irregular, and at two sites the largest concentrations of gas hydrate (>80% of the pore volume in sections several tens of meters thick) occur at shallow depths of less than 100 mbsf (sites U1326 and U1327) (Riedel et al., 2006a).

Focused flow within cold vents represents the other end-member mechanism for hydrate formation where the local hydrate concentrations may be very high. It is unknown how important these cold vents are in the total fluid-carbon-gas budget in an accretionary prism (Riedel et al., 2006a). There are many indicators of methane venting at the seafloor: gas-bubble plumes in the water column (Suess et al., 2001; Vidalie, 2007; E. Willoughby, personal communication, 2007), chemosynthetic communities (Lewis and Cochrane, 1990; Riedel et al., 2006b), massive carbonate crusts (Ritger et al., 1987), near-seafloor gas hydrate (MacDonald et al., 1994; Suess et al., 2001; Chapman et al., 2004), and seabed pockmarks (Hovland et al., 1993; Vogt et al., 1999). Seismically, other indicators are seismic wipeout zones, or subvertical zones of reduced reflectivity (Riedel et al., 2002), shallow/elevated BSRs (Wood et al., 2004; Tréhu et al., 2003), and local velocity pull-up/pull-down features (Scholl et al., 1978; Lee et al., 2005).

Different mechanisms have been proposed for the origin of the seismic wipeout and for the nature of the fluid venting. The mechanism must explain how gas or gas-saturated fluid reaches the seafloor without forming hydrate as it enters the stability field 250 m below the seafloor. Wood et al. (2002) propose that warm rising fluids significantly perturb the base of gas hydrate stability upward to near the seafloor, and the entire blank zone is from free gas beneath the elevated BSR. However, heat-flow measurements have not shown a current thermal anomaly over the Bullseye vent structure, and Riedel et al. (2002) suggest that much of the wipeout is caused by near-surface carbonate or by the massive hydrate layer at the surface; additional blanking may result from scattered accumulations of hydrate in the subsurface. Zühlsdorff and Spiess (2004) argue that the blanking zones below vents are produced by free gas bubbles within natural hydraulic fractures. Liu and Flemings (2007) postulate that the base of hydrate stability moves upward in the vent structures because of the progressively higher salinities generated by the salt that moves into the residual pore water as hydrate is formed. Haacke et al. (2008a) show how this model can be applied to structures off Korea.

We report on a deep-towed high-resolution multichannel seismic survey (DTAGS2), carried out in 2002 over this cold vent field near site U1328 (Figure 1). The project was a collaboration among the University of Victoria, the Geological Survey of Canada, and the U.S. Naval Research Laboratory (NRL, Washington, D.C., and Stennis Space Center, Mississippi, U.S.A.). The data were obtained using the high-resolution NRL deep-towed acoustic/geophysical system (DTAGS) on the CCGS *John P. Tully*. The primary goals were to obtain high-resolution structural details at a cold vent field, including the extent of associated methane gas hydrate and underlying free gas, and to determine the associated seismic velocities that could be used to estimate gas hydrate concentrations.

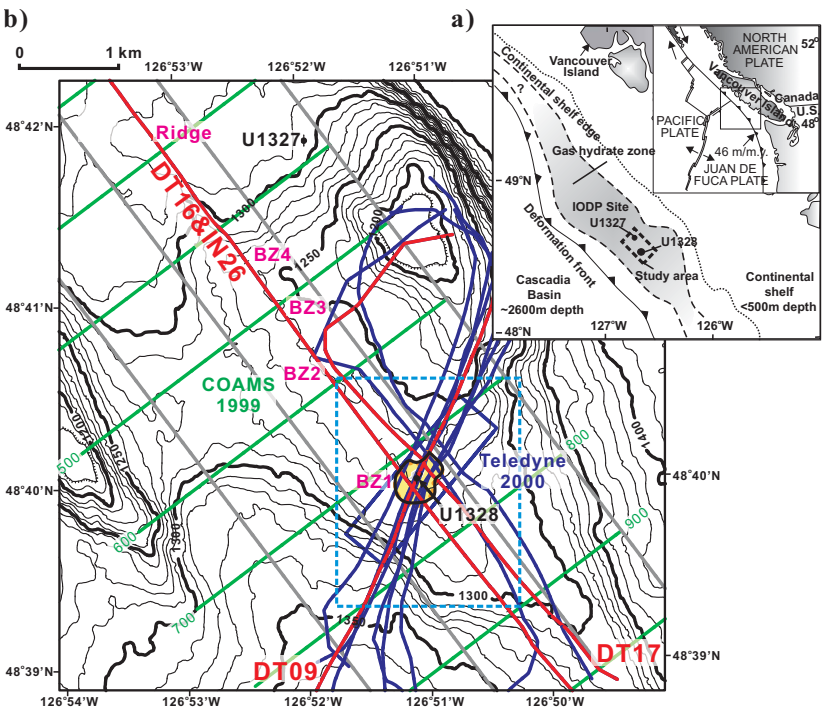

Figure 1. (a) General tectonic setting of northern Cascadia margin. The dashed box indicates the study area of the detailed survey location in the region of the Bullseye vent field on the midslope region offshore Vancouver Island. (b) Location of 2002 DTAGS2 lines, Teledyne 2000 single-channel 3D grid (blue box) and COAMS 1999 multichannel grid (green and gray grid) around the Bullseye vent (yellow area with black outline). The four seismic blanking zones are also labeled with BZ1-4 as well as on Figure 14. The dashed cyan box outlines the area showing details in Figure 2. The bathymetry contour interval is 10 m, using the data from a Sonne cruise SO 149 in 1999 (Zühlsdorff et al., 2002).

DTAGS SYSTEM AND DATA ACQUISITION

The DTAGS system consists of a Helmholtz resonator source and a solid-core hydrophone streamer with two subarrays containing 24 omnidirectional hydrophones (Table 1) (Gettrust et al., 2004). The advantages of DTAGS over sea-surface systems are that it provides a source that is highly reproducible because it is solid state and there is no cavitation and high vertical resolution resulting from the high frequencies (220–820 Hz). The wavelengths are less than 6 m, much shorter than the 25–50 m associated with typical conventional multichannel seismic data with frequencies of 30–60 Hz. Another advantage is greater sampling in wavenumber space using shorter hydrophone arrays with small receiver spacing. In addition, a smaller Fresnel zone resulting from the deep-tow geometry provides a much shorter distance from the source to the re-

flectors. Furthermore, the deep-towed system records wider-angle reflection data and may provide useful information for moveout velocity and amplitude variation with offset (AVO) analyses (Gettrust et al., 1999, 2004). The major disadvantage is that the high-frequency, short-wavelength data require very accurate positioning of source and receivers for stacking and velocity analyses. The special processing required to establish the position of the source and each receiver sensor is a primary focus of this study.

During the 2002 DTAGS2 experiment, 11 lines crossed the Bullseye vent field (Figure 1b): seven southwest-northeast lines plus four southeast-northwest lines in the direction. The source was fired every 30 s, or ~30 m at a nominal ship speed of 2 knots. Using a 24-bit Sigma-Delta converter at each hydrophone, data were digitized at a sampling interval of 0.5 ms with a recording length of 1.9 s, including a 250-ms delay (Spence et al., 2002).

Four engineering nodes were on the streamer: node 1 was on the source at 0 m, and the other three were on hydrophone channel 28 at 138 m, channel 38 at 288 m, and channel 48 (the last channel) at 438 m. These engineering nodes recorded pressure (depth) and temperature, as well as the seismic signal. The pressure gauges at the four nodes yielded several pressure readings during the 30 s between shots. These pressures were averaged over the shot interval, converted to depth (including a local density correction based on a temperature measurement in the node) and placed in the SEGY trace header. Normally these depths are more accurate than the values calculated from traveltime and estimated water velocity. Figure 3 shows the depth variations of the nodes during survey line DT09.

Although the navigation of the ship (differential GPS, or DGPS) provided positions with antenna position uncertainties close to 1 m,

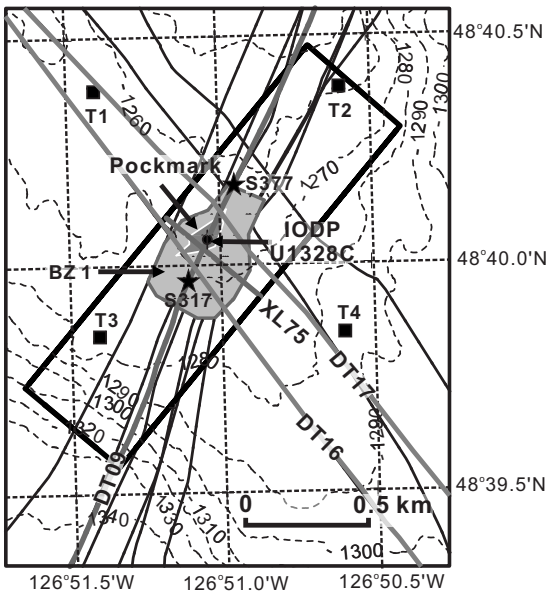

Figure 2. Map view of the Bullseye region, associated with seismic blanking zone BZ1 (light gray); massive hydrate was recovered in shallow piston cores within the dark gray region (pockmark). The 2002 DTAGS2 survey lines are indicated by solid black lines. The thick box outlines the area of the 2000 Teledyne single-channel pseudo-3D grid. The thick gray lines indicate the seismic sections showing hydrate cap details in Figures 9–12. The locations of two velocity analyses, S317 and S377, are labeled with black stars. Transponder deployment (T1T4) during this experiment and IODP site U1328 are also labeled.

the DTAGS was towed behind the ship at horizontal distances of up to 1 km, and its horizontal distance could vary hundreds of meters from the track of the ship within a survey. Therefore, navigation was also determined acoustically with a transponder net deployed in 2001 in preparation for the DTAGS2 experiment in 2002.

A four-element long-baseline (LBL) acoustic seafloor array was arranged on four corners of a square with sides about 1 km long (Figure 2). A fifth relay transponder, or rover, was attached to the DTAGS source. The DGPS from the ship and the known locations of transponders on the seafloor were used via acoustic traveltimes to determine the position of the relay transponder. During operation, navigation using all four transponders was possible within the LBL array, usually out to 100–200 m beyond the array boundaries but sometimes up to 1 km outside the array. WINFROG commercial navigation software calculated real-time positions of the ship and rover. This allowed a real-time visual assessment of the positions of the ship and rover (Spence et al., 2002).

Unfortunately, many irregular jumps in the rover navigation, mainly from a large number of repeated readings and acoustic interference from strong noise sources, made it very difficult to position the DTAGS accurately and limited the value of using the acoustic

Table 1. DTAGS configuration during the 2002 DTAGS2 cruise.

Characteristic	Details
Acoustic array	24 channels, group spacing of 3 m
	Minimum offset: 9 m
	Maximum offset: 78 m
	First two channels dead
Geophysical array	24 channels, group spacing of 15 m
	Minimum offset: 93 m
	Maximum offset: 438 m
Source	Helmholtz resonator generating 250-ms-long sweep (220–820 Hz)
Source strength	~200 dB/1 Pascal @ 1 m, sufficient to penetrate upper 400 m of sediments

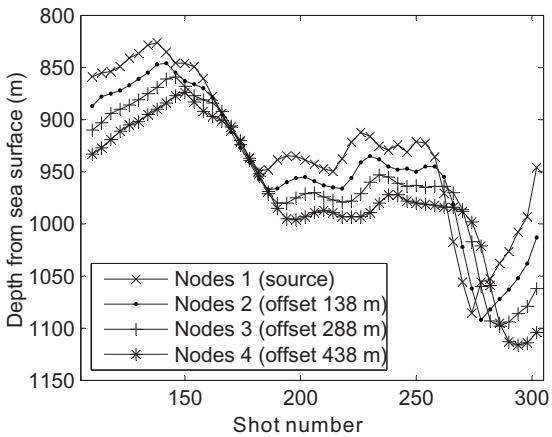

Figure 3. The depth variations of the four nodes on DTAGS streamer along survey line DT09 (Figures 1b and 2), showing an example of nonlinear variation of array geometry.

transponder net. An effort was made to correct the rover navigation manually in postcruise processing by eliminating duplicate readings and acoustic positions that clearly were in error and interpolating between reliable positions. The corrected rover navigation still was not accurate enough for precisely stitching DTAGS shot images as originally designed, but it provided more reliable absolute rover 3D positioning than navigating the ship alone.

DATA PROCESSING

Source crosscorrelation and spectral balancing

The vibroseis-like source of DTAGS is a 250-ms-long sweep frequency-modulated sinusoid that is tapered on both ends. The initial step in processing the DTAGS data was to crosscorrelate the field recordings with the source signal. Although deconvolution (frequency-domain division) gives a better spectrum than correlation in theory, correlation (frequency domain multiplication) is in practice more stable because division by values near zero will produce unreasonably large amplitudes at the corresponding frequencies. An approximate pilot sweep was obtained from the direct wave recorded at the near-offset hydrophone, about 15 m from the source; previous studies by Chapman et al. (2002) show that this approach gives the clearest seafloor and deeper reflectors.

For the broadband signals in the DTAGS data, spectral balancing achieved better image quality than the popular Butterworth filter. Spectral balancing is a zero-phase deconvolution, effected by spectral equalization in the selected frequency domain; we assume no frequency dispersion or associated phase changes. In practice, the 2002 DTAGS data show improved image quality after applying spectral balancing with selected band-pass frequency limits of 220–250 to 510–545 Hz: some seismic events were enhanced by compressing the wavelet slightly, and a relatively clean image was achieved by rejecting some of the higher frequencies in the spectrum.

Array geometry estimation

Although the near-bottom configuration and wide high-frequency bandwidth of DTAGS allow much better resolution of the subseafloor structures in the upper 400 m, the system has three special problems for data imaging and velocity analysis: (1) shot-to-shot variations in source position are poorly constrained; (2) difficulty maintaining a horizontal array shape during towing, so receiver positions for each shot are poorly constrained; (3) short 26-m wavelengths that require very precise positioning and time alignment to determine moveout velocity. Significant nonlinear variations in array geometry, particularly in the longer geophysical array (Table 1), occurred throughout most of the DTAGS experiment (Figure 3). Compared to an optimal horizontal system, these variations caused considerable reflection-time errors and required accurate correction before conventional seismic processing could be applied.

In earlier DTAGS experiments (Rowe and Gettrust, 1993), depth readings from the few sensors located along the streamer were used to interpolate the approximate array geometry linearly. However, these interpolated values were not accurate enough to calculate satisfactory time corrections for the nonlinear cable geometry. The DTAGS seismic signal normally included strong sea-surface reflections (SSR), which provide more accurate two-way time and consequently depth for each hydrophone group, assuming constant water velocity during a shot interval. Walia and Hannay (1999) determine array geometry by using SSR times at six receiver channels and interpolate times using a cubic spline for the remainder of the channels. They then correct traces to a single constant datum for the whole survey line; this can produce large moveout velocity errors if the depth corrections are several tens of meters.

We extend the work of Walia and Hannay (1999) to achieve optimal cable geometry and more accurate time corrections. Our method uses a genetic algorithm inversion to find positions of the sources and receivers, using known node depths and manually picked times for the direct arrivals and the reflections from the sea surface. Our method also uses a floating datum system to reduce errors during time correction.

We determined the cable geometry in the 2D vertical plane because no information on cable feather angles was available. As the first step, the SSR and direct-arrival times were picked on the trace envelope instead of the raw waveform because the crosscorrelated wavelet was inconsistent from trace to trace for the DTAGS high-frequency data, caused by the water-wave roughness of the sea surface. We picked arrival times at the first zero crossing rather than the envelope maximum, which shifted with offset and shot depth because of phase changes. The picked times were then shifted about 7 ms downward to the approximate locations of envelope peaks. Note that the direct arrival wavelet is present only in the last 24 receivers at the farthest offset as a result of the 250 ms delay in recording.

The second processing step was to calculate the largest horizontal offset and interpolation velocity for each shot. Because one of the engineering nodes was attached to the last receiver, it was a unique point on the cable at which the depth reading, SSR time, and direct-arrival time could all be obtained. Thus, the horizontal far offset of the cable (x') can be determined, as well as the nominal water velocity (V_w, assumed to be constant in the water mass above the array) to be used for interpolating SSR times to all receivers for each shot gather, using the following equations:

$$x' = \sqrt{(T_{\text{direct}} V_w)^2 - (d_r - d_s)^2}, \tag{1}$$

$$V_w = \sqrt{\frac{4 d_r d_s}{T_{\text{SSR}}^2 - T_{\text{direct}}^2}}, \tag{2}$$

where T_{SSR} is the two-way time of the sea-surface reflection, T_{direct} is the one-way time of direct arrival, and d_s and d_r are the depth of the source and the receiver, respectively, calculated from temperature-compensated pressure measured at the far-offset node.

Assuming that the depth readings are accurate and the cable geometry is smooth to first order at locations of the engineering nodes, the positions of traces other than the last one can be predicted by using their SSR times to invert the whole cable geometry to a polynomial spline shape. For any shot gather, once the interpolation velocity V_w and farthest horizontal offset x_{48} at channel 48 of node 4 are determined by equations 1 and 2, a genetic algorithm (GA) method provided by MATLAB (The MathWorks, Inc.) is used to determine the horizontal offsets for the other two middle nodes (x_{28} of channel 28 and x_{38} of channel 38) and the vertical depths at three positions: (d_{24}, d_{33}, and d_{43} at channels 24, 33, and 43). The optimization function of the GA method is to minimize a fitness value defined as the sum T_t of residual SSR times between the calculated T_{SSR} and the picked T_{pick} times for all channels (channel 148) within a shot gather:

$$T_t = \sum_{i=1}^{48} |T_{\mathrm{SSR},i} - T_{\mathrm{pick},i}| \quad (3)$$

and

$$T_{\mathrm{SSR},i} = \sqrt{\frac{x_i^2 + (d_i + d_s)^2}{V_w}}. \quad (4)$$

where x_i is the horizontal offset of channel i from the source, d_i is the vertical depth of channel i from sea surface, and d_s is the vertical depth of the source from sea surface.

For each generation, the GA method produces a population of 50 individuals from the previous generation. Each individual is characterized by the five variable values; the horizontal offsets of the remaining receivers are linearly interpolated between the four nodes, and then the depths are calculated using a polynomial fitting curve. Order three and order five polynomials are tested. A new fitness value T_t (Equation 3) is calculated from the new SSR times for each individual, and the overall population is assessed to make the next generation.

The GA used for DTAGS cable inversion continues to produce generations until there is no further improvement on the fitness value T_t. The GA process takes 1030 s for one shot gather, using a 1.4-GHz personal computer. The typical minimum fitness value T_t is less than 40 ms. Thus, the average SSR residual (T_t/48) between the GA inverted time and the picked seismogram time is less than 1 ms, which is smaller than the picking error and represents appropriate convergence of the inversion process.

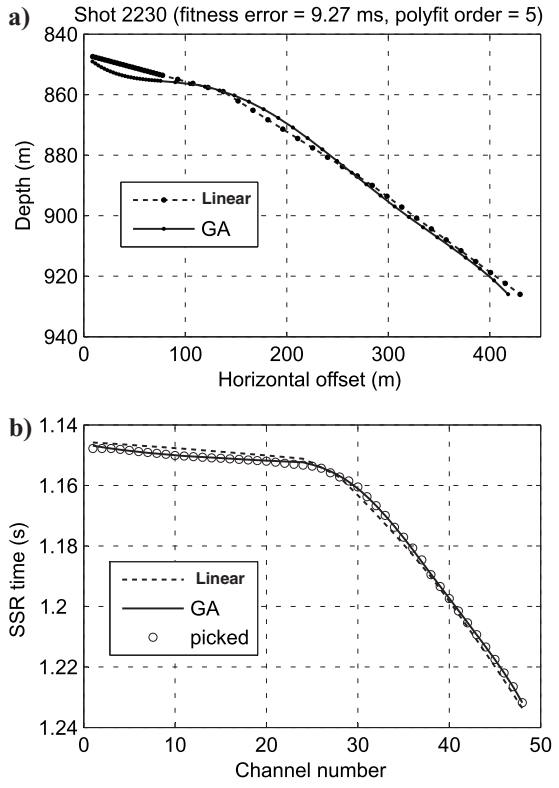

Figure 4. Comparison of the GA inversion result and those from a linear cable assumption for shot 2230 of survey line DT10. (a) The GA inverted cable (solid line) has a more naturally curving geometry than the linear algorithm (dashed line with dots), which has straight lines between cable nodes. (b) Recalculated SSR times from inverted cable geometry (solid line) have much smaller misfit than the simple linear cable assumption (dashed line) when compared to the actual picked SSR times (open circles).

For shot 2230 of survey line DT10, the GA inversion results are compared to those using a linear cable geometry assumption. A more naturally curving cable was achieved using the inverse method (solid line, Figure 4a). Note that the cable depths varied from 850 m at the first receiver to 930 m at the last receiver over a horizontal distance of approximately 420 m, and the 35-m mismatch between the GA inverted geometry and the linear cable assumption produced a 34-ms difference in corresponding SSR times (Figure 4b). The DTAGS cable was closer to the seafloor than to the sea surface, so the time difference between the GA method and linear assumption will be even larger for sediment reflections. Considering that a 1-ms time difference will produce a noticeable mismatch for DTAGS imaging, the GA inverted cable geometry is more reliable than the one using a linear assumption.

Datum correction and NMO calculation

Once the cable geometry is accurately known for each shot, time corrections are computed to move reflection arrivals on the original curved array to the corresponding times on a simulated horizontal system. We assume straight raypaths to a subseafloor sediment interface, which should be an adequate approximation. Figure 5 illustrates that the original raypath AB + BC from the source to the last receiver could be approximately replaced by the raypath A′B′ + B′C′, with both source and receiver on a horizontal datum at depth H_d, given by the mean value of source-receiver depths, and with the source-receiver distance corrected to the original offset x.

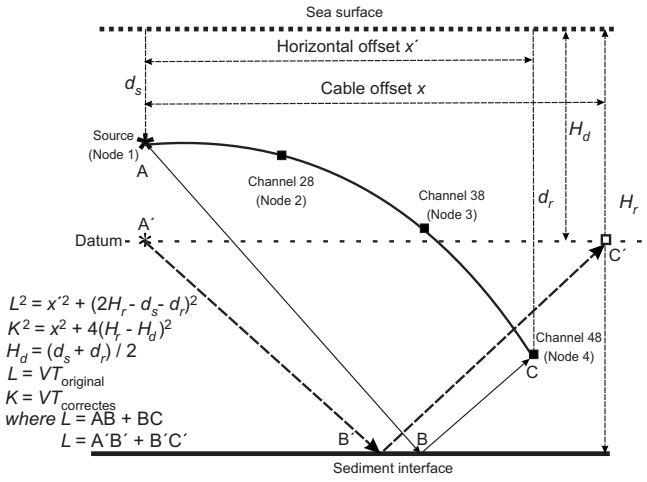

Figure 5. Illustration of time correction for source/last receiver pair. The original raypath AB + BC from source to the last receiver reflected at point B on the sediment interface is replaced, after time correcting, by the new raypath A′B′ + B′C′ for which the source and receiver are at the same datum at their mean depth and their distance is corrected to their original offset x on the cable. V is the average velocity calculated previously, estimated from the water velocity and a sediment velocity structure assumption; T_{original} is the original twt of AB + BC; $T_{\mathrm{corrected}}$ is the twt of A′B′ + B′C′ after time correction; H_d and H_r are the depth of the datum and sediment reflector, respectively, measured from sea surface; d_s and d_r are the depth of the source and the receiver, respectively.

The raypath changes for varying incident/reflection angles at different reflection depths, so the time correction is calculated by marching a small time window iteratively through the seismic trace data. The previous study by Walia and Hannay (1999) showed that a window length of 20 ms is adequate. At each iteration, the depth H_r of the reflector, corresponding to the two-way time T_{original} for raypath AB + BC, is calculated assuming an approximate velocity profile (e.g., from nearby multichannel or refraction surveys). This depth H_r is then used to predict the expected time $T_{\text{corrected}}$ for the horizontal source-receiver system at the datum depth H_d. Time corrections ($T_{\text{corrected}}$) for the top and bottom of the marching window are calculated separately, and the data in the original window are stretched/contracted and time shifted to fit the new window accordingly. The time correction calculations are differential in nature, so the errors are only weakly dependent on the velocity profile (Walia and Hannay, 1999), particularly because the DTAGS signal penetration is limited to the upper 400 m of sediments. Thus, it is adequate to use a very approximate velocity profile, such as a constant average velocity over the raypaths estimated by combining the water and shallow sediments (e.g., 1600 m/s).

Unlike the constant datum depth used for the whole survey line by Walia and Hannay (1999), an individual datum was chosen at the mean depth of each source and receiver pair. That is, a floating datum system was used in this study not only for different shot instants but also for different receivers within the same shot gather.

Once the time corrections for source-receiver pairs have been applied, an NMO process is used to shift traces to equivalent vertical incidence using constant seawater velocity. For the DTAGS imaging, we mainly used the nearer-offset dense acoustic array for which the moveout is quite small and using water velocity provides a reasonable image, especially for seafloor alignment. For comparison with reflection images collected with surface source and receivers, the DTAGS data are finally corrected to put shot and receiver at the sea surface by shifting the trace downward by a two-way time at seawater velocity for the vertical raypath from the sea surface to the datum depth. A few shot gathers are shown in Figure 6 before and after

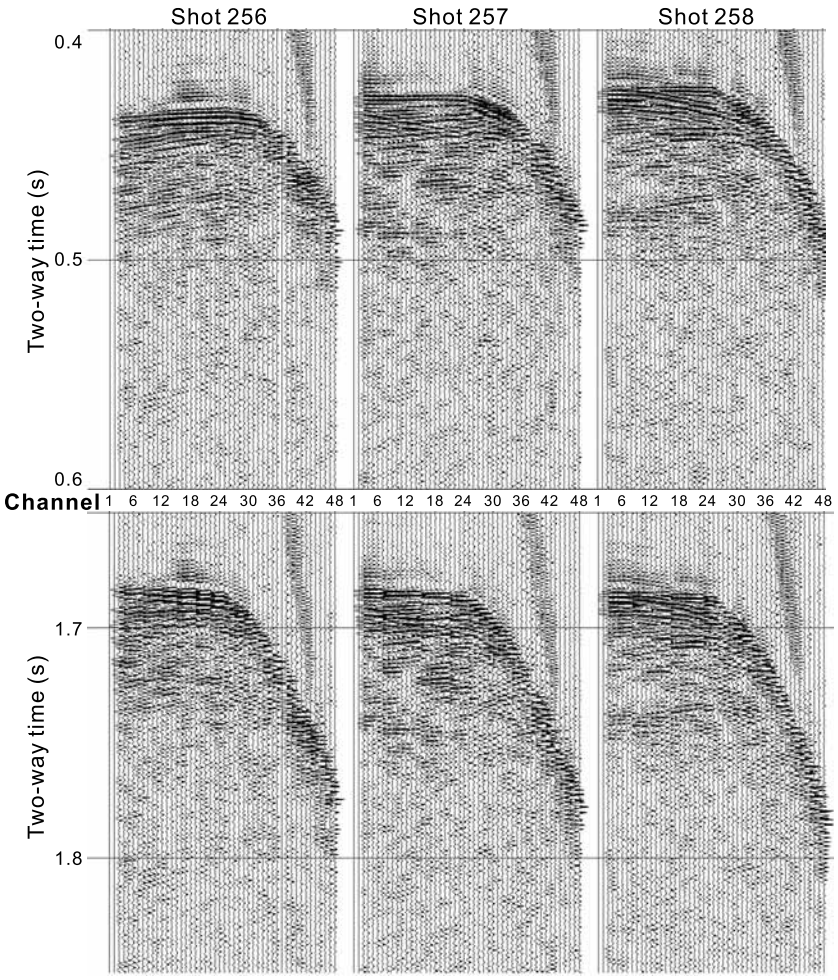

Figure 6. Shot gathers from the deep-tow array before (top) and after (bottom) time corrections for variations in both receiver array shape and shot depth. The bottom images have been corrected to the vertical traveltime from the sea surface to the seafloor, and the traces are not equally spaced in offset: the first 24 channels are the acoustic array (channel 124, spacing 3 m), and the remaining 24 channels with much larger moveout corresponds to the geophysical array with longer offset (channel 2548, spacing 15 m) (see Table 1).

time corrections for variations in receiver array shape and source depth; the true reflection hyperbolas have been restored, and the sources are at a consistent depth.

DTAGS data imaging

To form the high-resolution seismic image, the time-corrected DTAGS data were passed to a receiver statics analysis and a shot image stitching process. To seek consistency along a seismic reflector, these calculations were based on crosscorrelations of trace envelopes.

To remove surface-consistent residual statics, receiver statics were first applied to minimize the difference between adjacent receivers. For a given shot, the trace envelopes of each adjacent receiver pair were crosscorrelated and the lag between the traces, corresponding to the maximum amplitude of the crosscorrelation, was determined. The mean value of these lags over all shots, after conversion to sample number or static time, was the relative statics correction for these two receivers. The calculated receiver statics were very small (<1 ms) because the maximum 15-m offset between receivers is small compared to the source Fresnel zone.

The major differences between two adjacent shot images are caused mainly by variations in the source spacing and source depth. Although the navigation of the ship provided estimates of ship position and speed, the source did not follow the motion of the ship precisely. With the source located at the end of a long tow cable, the source would rise or fall in the water column as the speed of the ship varied, and the horizontal distance of the source behind the ship also varied. To constrain this variation in source position, the large overlapping area between two adjacent shot images was used to calculate vertical shot statics and the optimal horizontal position for image stitching.

Although the nominal ship speed was approximately 2 knots, such low speeds are difficult to maintain at a constant. The ship speed varied from 1.5 to 3 knots over most of the survey, with corresponding shot spacing variations of 2145 m for a nominal shot interval of 30 s. Because the maximum trace offset is 438 m (Table 1), the reflection midpoints extend out to 219 m from the source. There is thus a significant overlap in common-reflection-point (CRP) position from one shot to the next, varying from 174 to 198 m.

The overlapping areas for adjacent shot images were compared CRP by CRP for shot spacing varying from 21 to 45 m with a stepping size of 3 m (corresponding to the spacing of the acoustic array). This produced a series of crosscorrelation seismograms for different overlapping areas, with each series characterized by a mean value and a standard deviation over all the picked trace lags: the sample numbers corresponding to the maximum amplitude of the crosscorrelation. The optimal shot spacing, providing the most similar overlapping image between adjacent shots, is the spacing with the smallest mean lag value. In calculating the mean lag, we rejected shot spacings for which the standard deviation was more than twice the smallest value of all standard deviations.

A 100% coverage image is formed using selected traces from the acoustic array only. The farther offset geophysical array traces and overlapping acoustic array traces are used for velocity analysis only and are not stacked in the image. For these larger-offset traces, errors in alignment and in NMO correction are larger than for the near-offset acoustic array, so the single-fold image has the greatest continuity in image stitching and the highest resolution in image quality.

The above process, using crosscorrelation lags among all CRP traces between adjacent shots, defines the optimal overlap in traces or the optimal horizontal shot position. To calculate the relative vertical shot statics correction for the 100% coverage image, only lags for the first three common traces were used. This process automatically stitched 80%–90% of the DTAGS shot images. Some additional manual adjustment for individual shots was required, particularly for low-grade shots where many empty or noisy traces existed.

There are two obvious advantages of this image stitching method. First, calculating relative shot spacing does not rely on any positioning information (e.g., GPS navigation, acoustic transponder net). Second, a more reliable CRP grouping could be achieved for the NMO velocity analysis.

The stitched DTAGS images using the above method have no information on geographic coordinates. To better correlate subseafloor features to seafloor topography, a stitched DTAGS image was aligned to the corresponding rover track by assigning the beginning and end of the image to the beginning and end of the rover track, and interpolating trace coordinates between the nearest rover coordinates. We estimate errors in absolute positions are about 2030 m, based on comparison with a single-channel seismic (SCS) grid collected in 2000. Figure 7 is an example of the final processed acoustic image of the 2002 DTAGS survey line DT09.

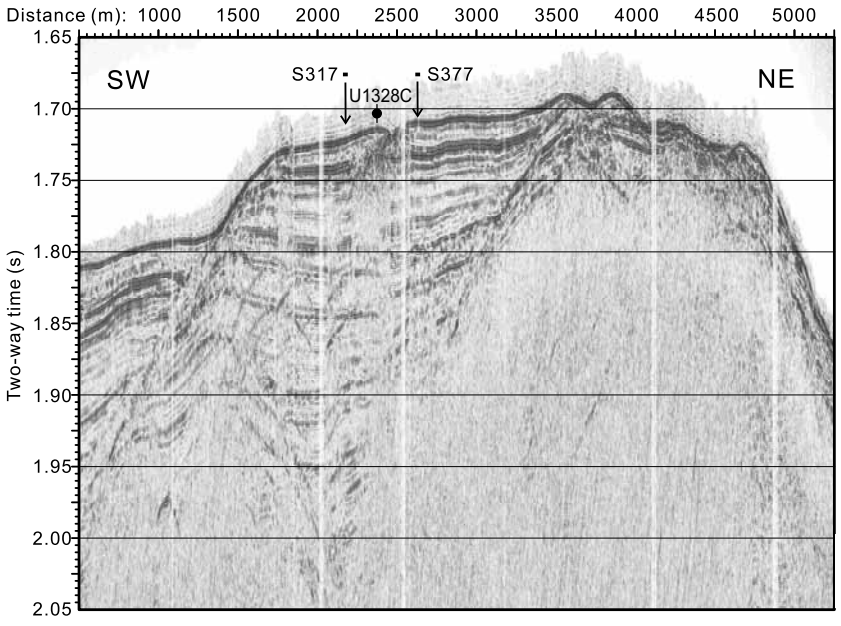

Figure 7. Acoustic image (100% coverage) of the survey line DT09, showing high resolution of subseafloor structures laterally and vertically. The location of IODP drill site U1328C is labeled. S317 and S377 label two locations where conventional velocity analysis was carried out.

Moveout velocity analysis

In the first attempt at velocity analysis of DTAGS data, Rowe and Gettrust (1993) used shot gathers. Velocity uncertainties were quite high because reflection points extended over a distance of >200 m.Sorting by common reflection point provides significant improvement in precision, but difficulties arise because of the irregular trace spacing resulting from variable ship speed and array geometry. In the DTAGS velocity study by Chapman et al. (2002), the shot spacing was estimated approximately only for line segments where ship speed was relatively consistent.

In the current study, more accurate CRP sorting was achieved by better determination of the optimal shot spacing from stitching adjacent shot images. The CRP bin size was set to 7.5 m, corresponding to the 15-m group spacing in the geophysical array. However, to increase signal-noise ratio for velocity analysis, four adjacent CRPs were grouped to form a CRP supergather. The effective bin size was then ~30 m, corresponding to the nominal shot spacing. So there are as many offsets in a CRP gather as in a shot gather.

Similar to the image process, time corrections for cable geometry and source-depth variations are required to obtain a horizontal system. For each CRP supergather, however, only a single reference datum is chosen at the average value of mean depths of each source-receiver pair; this is adequate for velocity analysis because the source depth varies by only a small amount over several successive shots. No depth shifting to the sea surface is needed. Once the cable geometry is corrected, the CRP supergather can be treated approximately as a conventional seismic data set, and standard seismic analysis routines can be used.

There are inadequate reflector horizons within the main vent structure for velocity determination, and velocity-depth estimates were obtained from CRP supergathers S317 and S337 of DTAGS2 survey line DT09 (Figure 7 and Figure 13) because they contain strong reflections that are nearly horizontal. They are centered approximately 180–270 m to the southwest and northeast sides of the center of the prominent seafloor pockmark (distance ~2460 m) associated with Bullseye vent. The reflection points for the CRP supergathers span about 25 m, from 2175 to 2200 m for S317 and from 2620 to 2645 m for S337.

Figure 8a shows prestack images of the constant-velocity gathers for CRP supergather S317. For a given reflection, we picked the rms velocity that best flattens the reflection. After applying NMO to the data, the final prestack image in the last panel shows all flattened reflections. From the monotonically increasing rms velocity profile, the corresponding interval velocities can be calculated using the Dix equation (Figure 9a). The deepest reflection occurs at 195 mbsf, slightly shallower than the expected depth of 210 mbsf for the BSR. For CRP supergather S377, similar NMO velocity panels were generated and interval velocities calculated (Figures 8b and 9b). The velocity analysis was limited to the upper 125 m because of weak reflectors at greater depth.

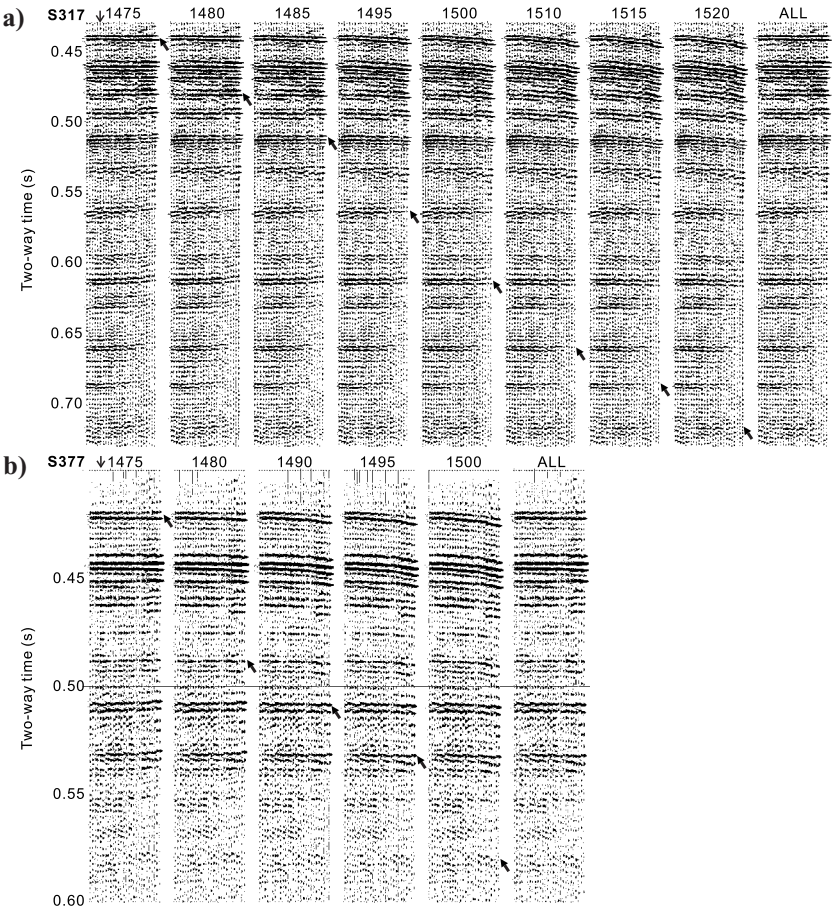

Figure 8. Constantvelocity gathers (CVG) at CRP supergather (a) S317 and (b) S377 on DTAGS2 survey line DT09. The rms velocity (in m/s) is shown at the top of each panel, and the bold arrow indicates the specific event that is best flattened with that velocity. The location where the acoustic array changes to the geophysical array is also indicated by a vertical arrow at the top of the first panel. The ALL panels show the resulting images after NMO with the final rms velocity profiles (Figure 9).

Velocity uncertainty estimation

The uncertainties of rms velocities from the constant-velocity gathers were about ±2.5 m/s given the velocity step size of 5 m/s. The associated uncertainties for interval velocities (thick solid lines in Figure 9) are significantly larger (±50 m/s to >100 m/s), particularly for thin sediment layers. The errors are in part caused by limitations in the datum correction and in the hyperbolic assumption and the associated assumption that interval velocities can be calculated from rms velocities using the Dix equation. During the datum correction (Figure 5), the true raypath ABC was replaced by an approximate one A′B′C′, and this approximation produced errors in source-receiver offsets and vertical time shifts. The largest errors occurred for the near-seafloor sediments, and the error decreased quickly as the depth of reflector increased. Other contributions to error are limitations in parameter estimation, notably source/receiver geometry and correction velocities for the water layer and sediment layers.

For reflection alignment in velocity analysis or for reflection stacking, the depth differences between the source and receivers should be less than

half the wavelength of the signal. Thus, for the high-resolution DTAGS with a midfrequency of 500 Hz, the vertical positions of the source and receivers must be known to within 1.5 m. The errors in the array geometry correction are difficult to quantify, but we can estimate the sensitivity of the velocity analysis to variations in source-receiver offset from the Norwegian-Greenland Sea.

With the inverted cable geometry of shot 196 on line DT09, we created a simple 1D model with water depth 1270 m, water velocity 1480 m/s, and uniform sediment velocity 1550 m/s. Using Snell's law, we traced rays from the source to the receivers from a sediment interface at 100 mbsf. With these synthetic traveltimes as input, we applied our datum correction followed by our NMO velocity analysis to calculate the sediment interval velocity. We then varied an individual model parameter to determine the effect on the inverted sediment velocity. We found a 5-m error in the maximum source-receiver offset caused a large interval velocity change of 20 m/s. We also discovered a 10-m/s uncertainty in water velocity only causes an interval velocity change of <3 m/s. Another discovery was that an uncertainty of 50 m/s in the sediment velocity used for datum correction only causes a change of 10 m/s in the inverted interval velocity. Finally, we learned a very large bias of 100 m from zero-error datum only causes an interval velocity change of <20 m/s. Thus, the most sensitive parameters for determining sediment velocity are those associated with cable geometry and datum correction.

DTAGS OBSERVATIONS AT BULLSEYE VENT

Imaging of hydrate cap

In July 2000, piston cores recovered massive hydrate at depths of 38 m below the seafloor (small dark gray patch within the light gray Bullseye vent area; see Figure 2). On a grid of SCS lines, a shallow reflector with a cap shape was interpreted as the top of massive hydrate on crossline XL75, oriented southeast-northwest (Figure 10; see Figure 2 for location). The hydrate cap deepens away from the center of the vent, and its depth matches well with the depths of the hydrate recovery at several piston core sites (Riedel, 2001; Riedel et al., 2002, 2006b).

The hydrate cap reflector is also seen on the 2002 DTAGS lines. Lines DT16 and DT17 cross the Bullseye vent and are oriented approximately southeast-northwest, close to the direction of the SCS crossline XL75 but offset by 50–100 m (locations on Figure 2). Also, DTAGS lines DT08, DT09, and DT10 cross the center of the vent southwest-northeast (Figure 2). On these lines, the top of the hydrate cap (black curves, Figures 11–13) was inferred from individual images and from intersections with other DTAGS lines. For comparison, the top of the hydrate cap was also inferred from the SCS grid (green curves). The DTAGS data and the SCS data do not give exactly the same depths for the hydrate cap; this is because their dominant frequencies are significantly different (400 Hz for DTAGS, 120 Hz for SCS), so amplitudes vary from different attenuation and different responses to velocity gradients and thin layers.

IODP site U1328 was drilled very close to line DT09 (Figure 2) within the Bullseye vent. DT09 shows highly resolved details of the sediment structure (Figure 13). The main vent is indicated by the seismic wipeout zone between 2250–2350 m distance. This blank zone disrupts the set of strong coherent reflectors that occur at ~1525 ms below the seafloor; however, it does not disrupt reflectors at the seafloor. There is a high reflectivity zone dipping southwest from a seabed depression, where the hydrate cap nearly intersects the seafloor, down to a depth of 2025 ms two-way time (twt) (~1025 mbsf) where it meets the blank zone. This high reflectivity feature may be a fracture zone that provides an oblique pathway for fluid flow in the main vent of the blank zone to bring gas and/or hydrate-coated bubbles to very near the seafloor. The top of the fracture

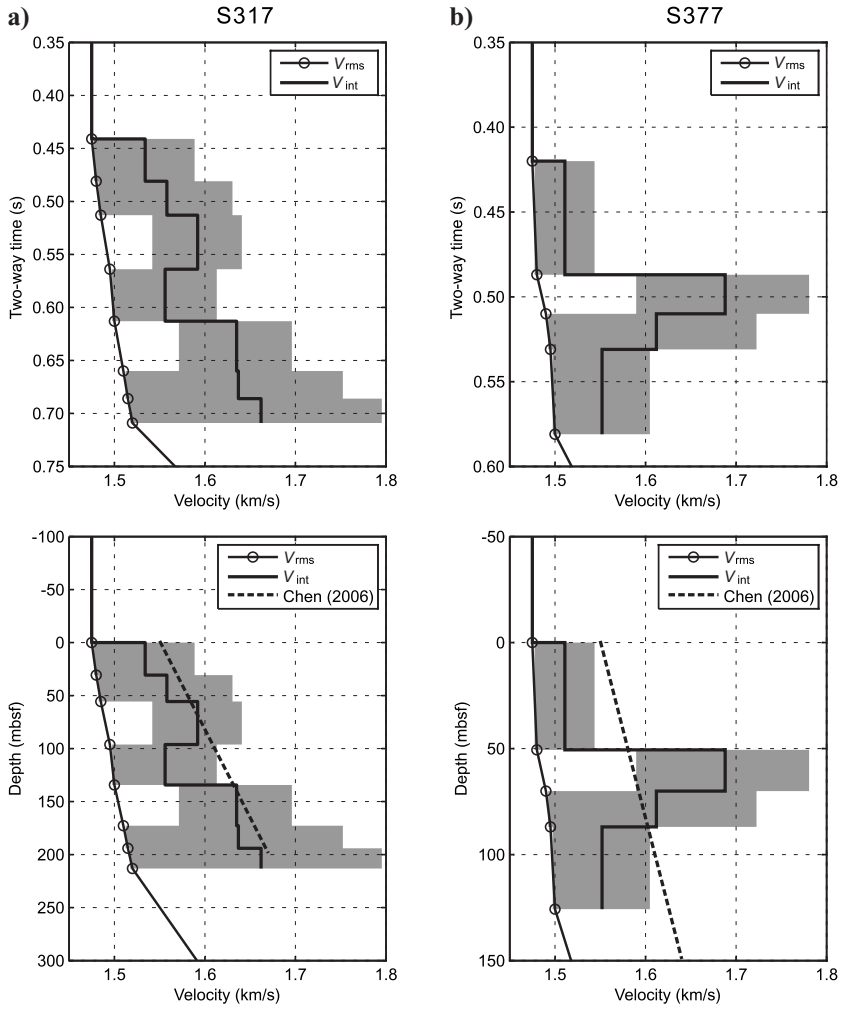

Figure 9. The rms velocity (V_{rms}) and corresponding interval velocity (V_{int}) in two-way traveltime and depth below seafloor, determined from constant-velocity gathers for CRP supergather (a) S317 and (b) S77 in Figure 8. The estimated error bounds for V_{int} are indicated by light gray shading. The no-hydrate reference velocity of Chen (2006) is marked by the dashed line.

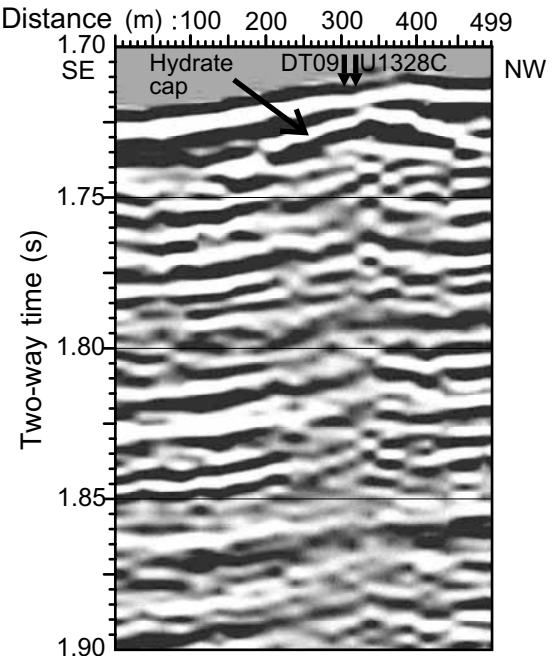

Figure 10. Southeast-northwest seismic section, showing hydrate cap details from Teledyne 2000 crossline XL75 (see Figure 2 for location). The locations of intersection with DTAGS line DT09 and nearby IODP site U1328 are also labeled. Note reduced seismic amplitudes below the hydrate cap (center of the vent).

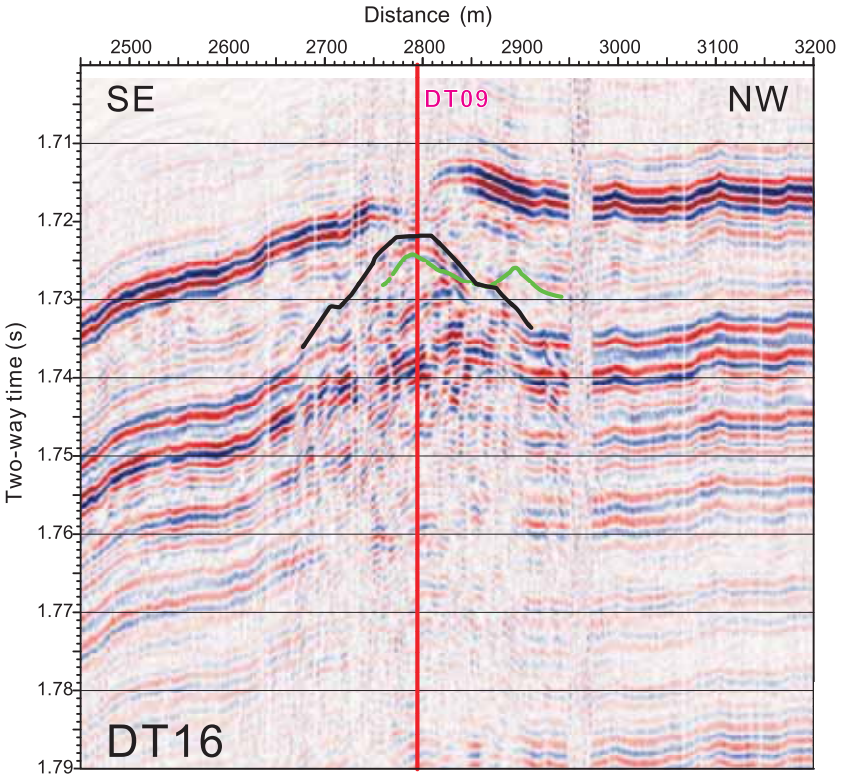

Figure 11. Southeast-northwest seismic section, showing hydrate cap details from DT16. The green curve is the hydrate cap location indicated from the Teledyne 2000 grid; the black curve is from the DTAGS line. The red vertical line indicates the intersection location with line DT09.

zone (black curve, Figure 13) corresponds to the top of the hydrate cap.

Blank zones on transit line DT16

Line DT16 continues as a long transit line extending to the northwest. The 1999 COAMS (Canadian Ocean Acoustic Measurement System) grid inline IN26 is coincident with DT16 (Figure 1). A combination of the surface-towed seismic data and the deep-towed DTAGS data is needed to provide sufficient information for proper imaging and interpretation. The high-quality seismic image of DT16 shows very detailed shallow sediment layers (Figure 14b), compared to the conventional multichannel seismic image of IN26 (Figure 14a). The IN26 image resolves four seismic wipeout zones as labeled in the slope sediments, likely representing fluid vent sites or protovents because not all of them extend upward to the seafloor. However, on the DT16 image, small diffractions are present at the seafloor for blank zones BZ2, BZ3, and BZ4, indicating the surface expressions of these ventlike features. The surface expression of the largest blank zone BZ1 (Bullseye vent) on DT16 is similar to a pockmark with a depression in the middle (Figure 14 and Figure 13b).

The second set of strong arrivals at about 20 ms two-way-time below the seafloor seems an apparent upward barrier for blank zone BZ2 (Figure 13b); the small pull-up or deformation that indicates the possible vent is restricted to depths below the strong reflectors. However, blank zones BZ3 and BZ4 partially cross this layer. The flanks of the blank zones show small-scale diffractions and, for blank zone BZ3, an apparent increase in seismic reflectivity for several reflections just outside the vent (Figure 14b).

The entire region from BZ2 to just northwest of BZ4 (Figure 14b) is a structural high. At the high-frequency range of DTAGS, the amplitude pattern in this region also contrasts with the surrounding area: reflections from about 1.8–1.87 s twt have enhanced amplitude, but the deepest prominent reflection between BZ1 and BZ2 (~1.95 s twt) does not continue beneath the structural high. The entire structural high region may contain greater amounts of hydrate than the surrounding area. Such an interpretation is consistent with the observations from controlled-source EM measurements (Schwalenberg et al., 2005), in which electrical resistivity beneath the entire BZ2 to BZ4 region is higher than that in the no-hydrate reference area.

A prominent small ridge lies at the foot of the slope, approximately 1500 m northwest of blanking zone BZ4. Significant seismic blanking occurs beneath the ridge. On neighboring COAMS high-frequency surface multichannel lines, the ridge with its associated blanking is buried at greater depths beneath less-deformed slope sediments (Riedel, 2001). Also, the DTAGS image DT16 shows a clear second coherent interface and a diapiric structure with uplifted sediments on both sides below the ridge. Thus, the blanking beneath the ridge may be the result of widespread penetrative deformation in the accreted sediments (Davis and Hyndman, 1989) and not from gas-charged or hydrate-filled sediments.

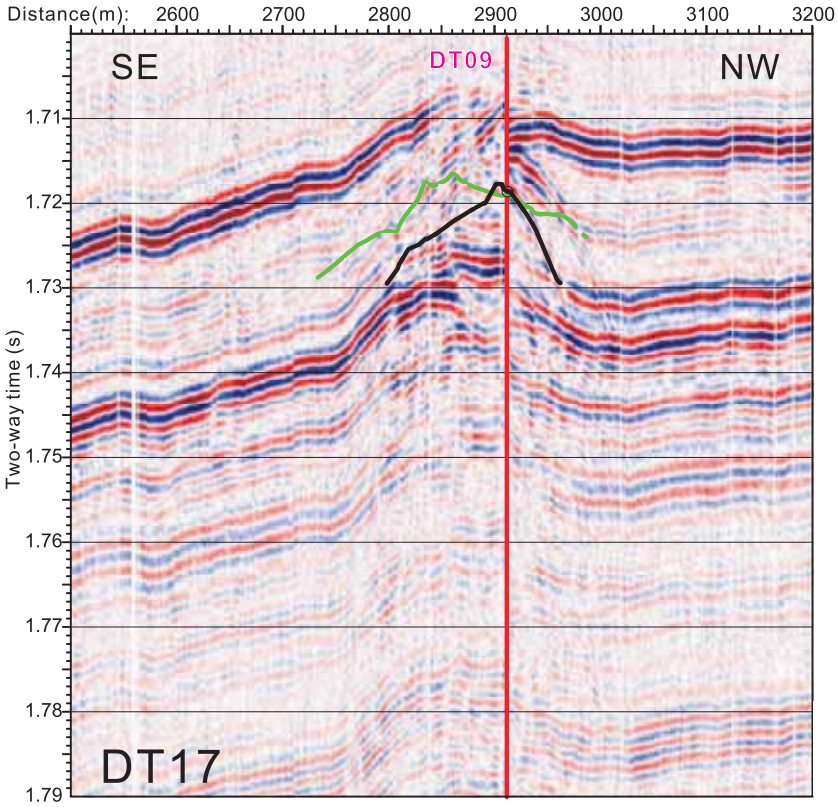

Figure 12. Southeast-northwest seismic section, showing hydrate cap details from DT17. The green curve is the hydrate cap location indicated from the Teledyne 2000 grid; the black curve is from the DTAGS line. The red vertical line indicates the intersection location with line DT09.

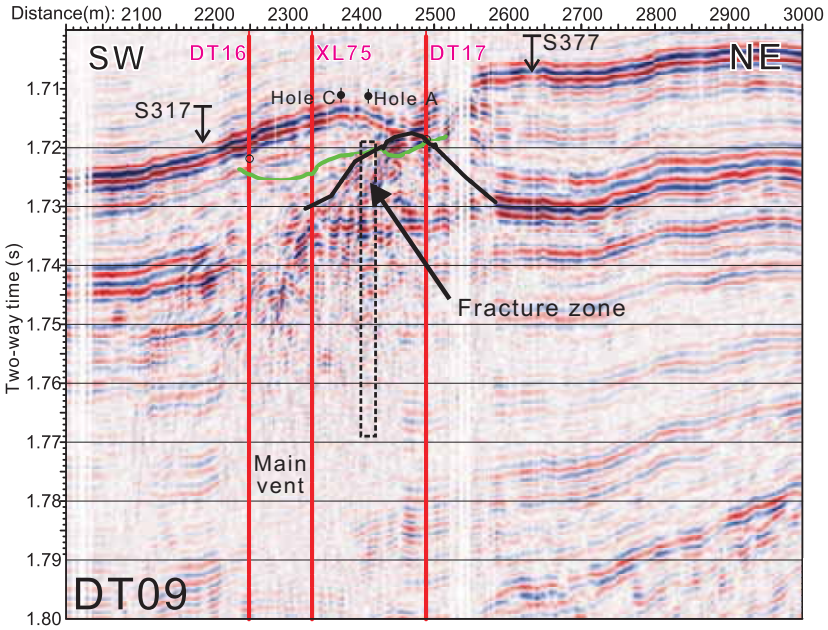

Figure 13. Southwest-northeast seismic section from DTAGS2 line DT09. The green curve is the hydrate cap location indicated from the Teledyne 2000 grid; the black curve is from the DTAGS line. The dashed black rectangle box indicates a layer with high hydrate concentrations from about 540 mbsf revealed by the resistivity log of IODP site 1328 hole A on this line (Figure 15). The top of this layer corresponds to the hydrate cap location. Maximum hydrate concentrations (~60%) correspond to a high-reflectivity fracture zone that projects to the seafloor. The two locations where velocity analyses were applied are also labeled (S317, S377).

Velocity results and comparison with IODP drilling

One of the objectives of the 2002 DTAGS survey was to investigate the properties of gas hydrate and associated BSRs. The P-wave seismic velocity of pure methane hydrate is 3650 m/s (Waite et al., 2000), significantly higher than the typical 1500–1600-m/s seismic velocity of sediments in the upper 200–300 mbsf if no gas hydrate is present. Thus, the measured seismic velocity of sediments containing hydrate provides a quantitative measure of the concentration of hydrate in the fluid pore space. Because of its deep-towed geometry and high-frequency content, DTAGS is well suited in principle to provide high-resolution, well-constrained velocity information about sediments containing hydrate.

At the two test supergather locations S317 and S377 (Figure 15), NMO-derived interval velocities can be compared to the sonic log and vertical seismic profile (VSP) from IODP site U1328 located within the Bullseye vent. The supergathers are located just outside the seismic wipeout region that characterizes the vent, less than 250 m from U1328 (Figure 7); unfortunately, because of the blanking, NMO velocities cannot be determined from within the vent itself because there are few clear reflectors. Also, downhole velocity information is available at site U1328 only for depths greater than about 60 m. NMO velocities have been measured at locations just outside the vent, from shallow depths (<60 mbsf) where no sonic velocities are available, down to depths that approach the BSR.

At supergather S317 just southwest of the Bullseye vent, interval velocities increase from 1.53 km/s in the first 30-m-thick layer below the seafloor to 1.67 km/s for the deepest layer that extends to 195 mbsf (Figure 15). These velocities are very close to the conventional multichannel estimate by Chen (2006) of the reference seismic velocity depth in this region for sediments containing no hydrate. The velocities are generally consistent with the sonic velocities from site U1328 and with the VSP values measured at depths >100 mbsf, which indicate an average velocity of 1645 m/s (Figure 15). In the two layers extending from 055 mbsf, there are normal velocities with no indication of high-velocity hydrate. At nearby site U1328, very high logging-while-drilling (LWD) resistivities were measured at depths of 540 mbsf (Figure 15), interpreted as a region of massive hydrate with saturations of 60%–80% of the pore space (Riedelet al., 2006a; Chen, 2006). This velocity analysis indicates that the shallow massive hydrate does not extend outside the vent to the southwest.

At supergather S377 on the northeast side of the seafloor pockmark, the derived interval velocities for most layers are consistent, within the estimated uncertainties, with the no-hydrate reference velocity profile of Chen (2006) and with the measured sonic velocities at site U1328 below a depth of about 60 mbsf (Figure 15). However, the interval velocity from 50–70 mbsf is 1.69 km/s. Although the estimated error bounds extend to just include the reference profile value, the preferred value implies a possible large velocity increase at this depth, with velocities 100 m/s greater than the reference. Us-

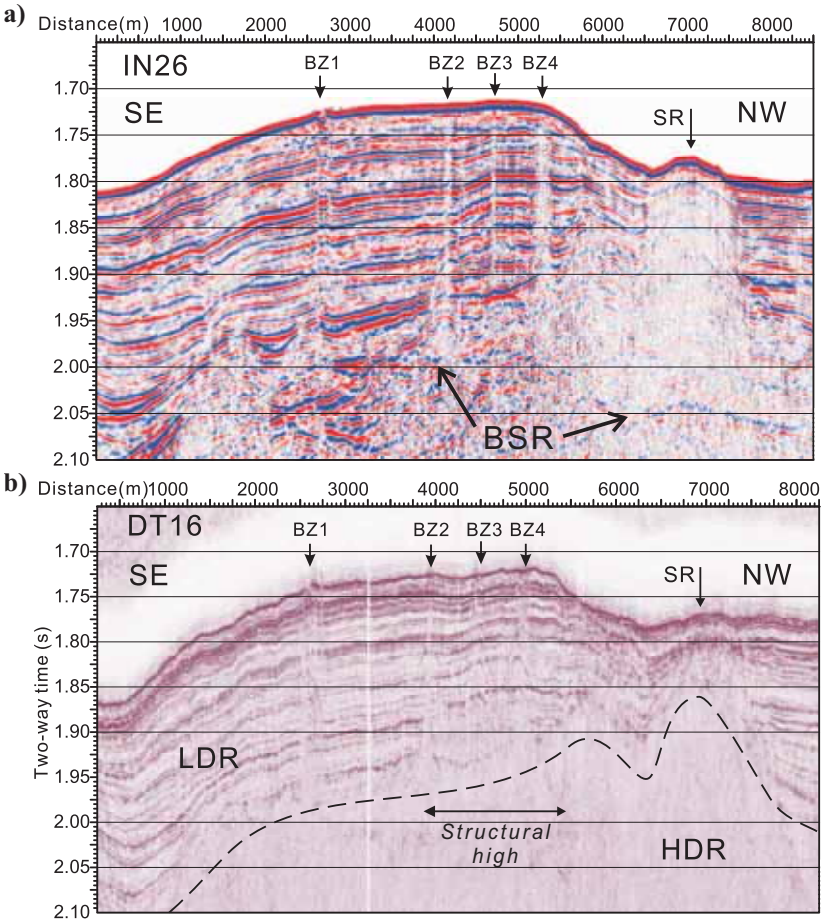

Figure 14. (a) Conventional multichannel seismic image of the 1999 COAMS grid inline IN26, providing a good comparison to the coincident DTAGS transit line DT16. (b) Acoustic image (100% coverage) of the 2002 DTAGS2 transit line DT16, showing fine layering of slope sediments, four seismic blanking zones BZ1-4, and a small ridge (SR) of accreted sediments, possibly diapiric. The dashed line indicates the boundary between the less-deformed region (LDR) of slope sediments and the highly deformed region (HDR) of older accreted sediments.

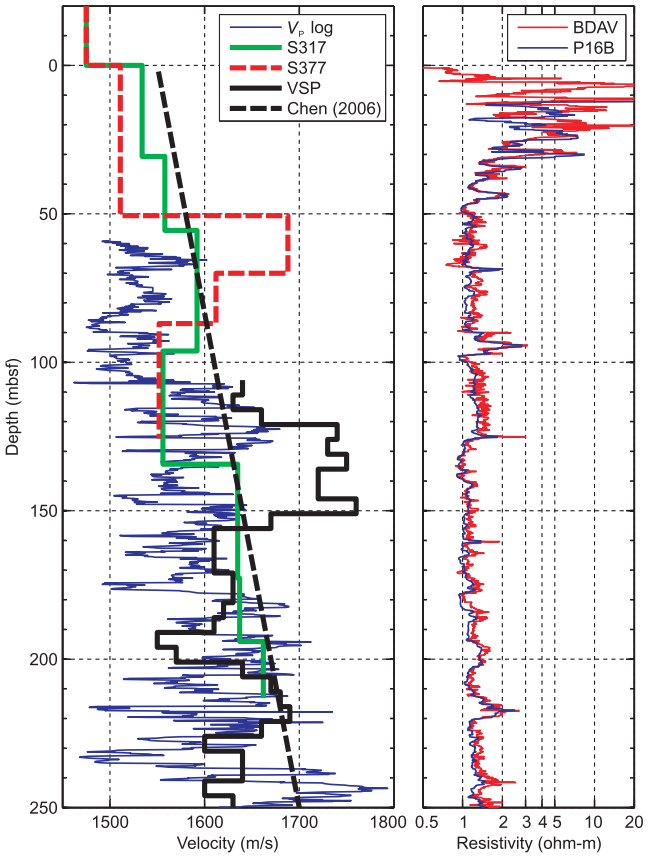

Figure 15. Comparisons of moveout velocity analysis results with U1328 drillhole logs. Velocity panel: sonic log (blue line), interval velocities of super-CRP S317 (thick green line) and S377 (thick red dashed line) (error bounds given in Figure 9), Bayesian inversion results of VSP starting from 106 mbsf (thick black line; associated errors usually a minimum of ±200 m/s), and the no-hydrate reference velocity of Chen (2006) (thick black dashed line). Resistivity panel: Button deep resistivity average (BDAV, red line) and phase shift resistivity blended, 16 inxhwa (P16B, blue line). The sonic log was recorded in hole U1328C, whereas resistivity logs came from nearby drillhole U1328A, 38 m northeast of U1328C (Riedel et al., 2006a).

ing the velocity-concentration models developed by Chen (2006) for nearby site U1327, we determine that the average hydrate concentration in this layer is 15%–20%.

CONCLUSIONS

The deep-towed DTAGS system has proven capable of imaging shallow structure beneath the seafloor at much higher resolution than surface-towed multichannel systems, but careful data analysis is required. A data analysis process was developed to determine the geometry of the receiver cable for each shot and to determine the position of the shots along a profile. Cable geometry is determined by inverting known node depths and picked traveltimes for the direct arrivals and reflections from the sea surface. For source positions, envelopes of overlapping traces between two adjacent gathers are crosscorrelated to find the optimal spacing between the shots. Although all traces along the 438-m cable are used for the source-receiver geometry and for subsequent NMO-velocity analysis, the highest resolution structural image is found using only the short-offset (78-m) high-density acoustic array. At the high-frequency short wavelengths of the DTAGS system, positioning is still inadequate for good trace-to-trace coherence using the full array.

The DTAGS images resolve multiple seismic wipeout zones in the midslope region of the Northern Cascadia margin. The blank zones likely represent fluid vent sites. A few may be protovents because not all of them extend upward to the seafloor. At the largest vent in the region, the Bullseye vent, the DTAGS data image is a 10 -m-thick high-reflectivity zone, extending from the seafloor to a depth of about 30 m and dipping seaward (southwest) at a small angle of 7°. This zone likely corresponds to the upper portion of the massive methane hydrate layer (~35 m thick) that has been piston cored and encountered at IODP site U1328. This high-reflectivity zone is interpreted as a complex near-surface hydraulic fracture system filled by hydrate, with gas-rich fluids fed from steeply dipping faults below it.

Interval velocities from NMO analysis of datum-corrected DTAGS data indicate that the shallow layer of massive hydrate does not extend outside the vent region because velocities in the upper 50 m just outside the vent generally are consistent with the reference velocity profile for sediments containing no hydrate. However, at a depth of 50–70 mbsf just to the northeast of the vent, interval velocities are approximately 100 m/s higher than the no-hydrate reference. This high-velocity layer may be a fluid-channeling fault zone. The high velocities suggest that hydrate concentrations in this layer are 15%–20% of the pore space.

ACKNOWLEDGMENTS

Captain Paul Frost and the crew of the CCGS *J.P. Tully* are gratefully acknowledged for their skill and flexibility. We sincerely thank Bob MacDonald of Pacific Geoscience Centre and Ivan Frydecky for their essential contributions to shipboard data collection. This research was supported by funds from the U.S. Naval Research Laboratory (ONR program element 61153N), the Geological Survey of Canada, and the Natural Sciences and Engineering Research Council. This paper is a Naval Research Laboratory contribution and a Geological Survey of Canada publication (Natural Resources Canada, Earth Science Sector publication 20080061). We are also grateful to Seismic Micro-Technology Inc. for the use of The Kingdom Suite.

REFERENCES

Chapman, N. R., J. F. Gettrust, R. Walia, D. Hannay, G. D. Spence, W. T. Wood, and R. D. Hyndman, 2002, High-resolution, deep-towed, multichannel seismic survey of deep-sea gas hydrates off Western Canada: Geophysics, **67**, 1038–1047.

Chapman, R., J. Pohlman, R. Coffin, J. Chanton, and L. Lapham, 2004, Thermogenic gas hydrates in the northern Cascadia margin: Eos — Transactions of the American Geophysical Union, **85**, 361.

Chen, M., 2006, Northern Cascadia marine gas hydrate: Constraints from resistivity, velocity, and AVO: M.S. thesis, University of Victoria.

Davis, E. E., and R. D. Hyndman, 1989, Accretion and recent deformation of sediments along the northern Cascadia subduction zone: Geological Society of America Bulletin, **101**, 1465–1480.

Gettrust, J., R. Chapman, R. Walia, W. Wood, D. Hannay, D. Lindwall, G. Spence, K. Louden, and R. Hyndman, 1999, High resolution seismic studies of deep sea gas hydrate using the DTAGS deep towed multichannel system: EOS — Transactions of the American Geophysical Union, **80**, 439–440.

Gettrust, J. F., W. T. Wood, and S. E. Spychalski, 2004, High-resolution MCS in deepwater: The Leading Edge, **23**, 374–377.

Haacke, R., K.-P. Park, I. Stoian, R. D. Hyndman, and U. Schmidt, 2008a, High flux venting in the East Sea, Korea, from analysis of 2D seismic reflection data: 6th International Conference on Gas Hydrates.

Haacke, R., G. Westbrook, and R. Hyndman, 2008b, Formation of the bot-

tom-simulating reflector and its link to vertical fluid flow: 6th International Conference on Gas Hydrates.
Hovland, M., A. G. Judd, and R. A. Burke, 1993, The global flux of methane from shallow submarine sediments: Chemosphere, **26**, 559–578.
Hyndman, R. D., and E. E. Davis, 1992, A mechanism for the formation of methane hydrate and seafloor bottom-simulating reflectors by vertical fluid expulsion: Journal of Geophysical Research, **97**, 7025–7041.
Lee, J. H., Y. S. Baek, B. J. Ryu, M. Riedel, and R. D. Hyndman, 2005, A seismic survey to detect natural gas hydrate in the East Sea of Korea: Marine Geophysical Researches, **26**, 51–59.
Lewis, B. T. R., and G. C. Cochrane, 1990, Relations between the location of chemosynthetic benthic communities and geologic structure on the Cascadia subduction zone: Journal of Geophysical Research, **95**, 8783–8793.
Liu, X., and P. B. Flemings, 2007, Dynamic multiphase flow model of hydrate formation in marine sediments: Journal of Geophysical Research, **112**, B03101, doi: 10.1029/2005JB004227.
MacDonald, I. R., N. L. Guinasso, Jr., R. Sassen, J. M. Brooks, L. Lee, and K. T. Scott, 1994, Gas hydrate that breaches the sea floor on the continental slope of the Gulf of Mexico: Geology, **22**, 699–702.
Riedel, M., 2001, 3D seismic investigations of northern Cascadia marine gas hydrates: Ph.D. dissertation, University of Victoria.
Riedel, M., T. S. Collett, M. J. Malone, and the Expedition 311 Scientists, 2006a, Proceedings of the Integrated Ocean Drilling Program, vol. 311: Integrated Ocean Drilling Program Management International, Inc.
Riedel, M., R. D. Hyndman, G. D. Spence, and N. R. Chapman, 2002, Seismic investigations of a vent field associated with gas hydrates, offshore Vancouver Island: Journal of Geophysical Research, **107**, 2200, doi: 10.1029/2001JB000269.
Riedel, M., I. Novosel, G. D. Spence, R. D. Hyndman, N. R. Chapman, and T. Lewis, 2006b, Geophysical and geochemical signatures associated with gas hydrate-related venting in the northern Cascadia margin: Geological Society of America Bulletin, **118**, 23–38.
Ritger, S., B. Carson, and E. Suess, 1987, Methane-derived authigenic carbonates formed by subduction-induced pore-water expulsion along the Oregon/Washington margin: Geological Society of America Bulletin, **98**, 147–156.
Rowe, M. M., and J. F. Gettrust, 1993, Fine structure of methane hydrate-bearing sediments on the Blake Outer Ridge as determined from deep-tow multichannel seismic data: Journal of Geophysical Research, **98**, 463–473.
Scholl, D. W., and A. K. Cooper, 1978, VAMPs — Possible hydrocarbon bearing structures in Bering Sea Basin: AAPG Bulletin, **62**, 2481–2488.
Schwalenberg, K., E. Willoughby, R. Mir, and R. N. Edwards, 2005, Marine gas hydrate electromagnetic signatures in Cascadia and their correlation with seismic blank zones: First Break, **23**, 57–63.
Spence, G., R. Coffin, and J. Hoehne, 2002, VENTFLUX2: Report of PGC01–03, C. C. G. vessel *John P. Tully*, 23 July-12 August 2001, cruise report: University of Victoria.
Suess, E., M. E. Torres, G. Bohrmann, R. W. Collier, D. Rickert, C. Goldfinger, P. Linke, A. Hauser, H. Sahling, K. Heeschen, C. Jung, K. Nakamura, J. Greinert, O. Pfannkuche, A. Tréhu, G. Klinkhammer, M. J. Whiticar, A. Eisenhauer, B. Teichert, and M. Elvert, 2001, Seafloor methane hydrates at hydrate ridge, Cascadia margin, *in* C. K. Paull and W. P. Dillon, eds., Natural gas hydrates: Occurrence, distribution and detection: American Geophysical Union Geophysical Monograph 124, 87–98.
Tréhu, A. M., G. Bohrmann, and the Leg 204 Scientific Party, 2003, Proceedings of the Ocean Drilling Program, Initial Reports Leg 204.
Vidalie, M., 2007, Methane plumes on the northern Cascadia margin detected by echo sounder: Internship Report, University of Victoria.
Vogt, P. R., J. Gardner, K. Crane, E. Sundvor, F. Bowles, and G. Cherkashev, 1999, Ground-truthing 11- to 12-kHz side-scan sonar imagery in the Norwegia-Greenland Sea: Part I: Pockmarks on the Vestnesa Ridge and Storegga slide margin: Geo-Marine Letters, **19**, 97–110.
Waite, W., M. B. Helgerud, A. Nur, J. C. Pinksto, L. Stern, and S. Kirby, 2000, Laboratory measurements of compressional and shear wave speeds through methane hydrate, *in* G. D. Holder and P. R. Bishnoi, eds., Gas hydrates: Challenges for the Future: Annals of the New York Academy of Sciences, 912, 1003–1010.
Walia, R., and D. Hannay, 1999, Source and receiver geometry corrections for deep towed multichannel seismic data: Geophysical Research Letters, **26**, 1993–1996.
Westbrook, G. K., B. Carson, R. J. Musgrave, and Shipboard Scientific Party of ODP Leg, 146, 1994, Proceedings of the Ocean Drilling Program, initial reports, 146 (Part 1).
Wood, W. T., J. Gardner, R. A. Hagen, R. B. Coffin, J. W. Pohlman, P. E. Hart, and D. R. Hutchinson, 2004, Modeling heat and fluid flux of seafloor mounds in the Gulf of Mexico: Proceedings, American Geophysical Union, Ocean Sciences General Contributions, Gas Hydrates I OS34B-08.
Wood, W. T., J. F. Gettrust, N. R. Chapman, G. Spence, and R. Hyndman, 2002, Decreased stability of methane hydrate in marine sediments owing to phase boundary roughness: Nature, **420**, 656–660.
Zühlsdorff, L., and V. Spiess, 2004, Three-dimensional seismic characterization of a venting site reveals compelling indications of natural hydraulic fracturing: Geology, **32**, 101–104.
Zühlsdorff, L., V. Spiess, T. Schwenk, N. R. Chapman, M. Riedel, and R. D. Hyndman, 2002, Multi-frequency seismic data in the vicinity of a gas hydrate site at the northern Cascadia accretionary prism: Proceedings of the 4th International Conference on Gas Hydrates.